Supplementary Material for "Hybrid Skin-Topological Effect Induced by Eight-Site Cells and Arbitrary Adjustment of the Localization of Topological Edge States"

Jianzhi Chen(陈健智)[1], Aoqian Shi(史奥芊)[1], Yuchen Peng(彭宇宸)[1], Peng Peng(彭鹏)[1], and Jianjun Liu(刘建军)[1,2*]

[1]Key Laboratory for Micro/Nano Optoelectronic Devices of Ministry of Education, School of Physics and Electronics, Hunan University, Changsha 410082, China
[2]Greater Bay Area Institute for Innovation, Hunan University, Guangzhou 511300, China

[*]Corresponding author. Email: jianjun.liu@hnu.edu.cn

A. Hamiltonian *H*

Figures 1(c) and 1(d) in the main text represent specific instances of intercell hoppings for a square unit and a rhombic unit, respectively. The signs of the hoppings change with the angles between the cells, aligning with the intracell hoppings (i.e., the two sites with specific numbers connected by a solid or dashed line in a cell, are also connected by a solid or dashed line between cells, respectively), as shown in Fig. A1.

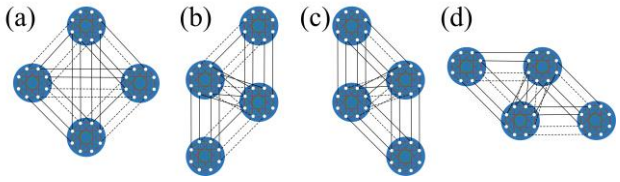

Fig. A1 (a) The other instances of intercell hoppings for the square unit in Fig. 1(c). The other instances of intercell hoppings for the rhomboid unit in Fig. 1(d): (b)–(d). The solid and dashed lines connecting cells represent positive and negative intercell hoppings, respectively.

According to Eqs. (2) and (3) in the main text, the intracell hopping in a cell in Figs. 1 and A1 is

$$T=\begin{pmatrix} 0 & 1+\delta_{21} & 0 & 1+\delta_{41} & 0 & -1-\delta_{61} & 0 & 1+\delta_{81} \\ 1-\delta_{21} & 0 & 1-\delta_{23} & 0 & 1-\delta_{25} & 0 & 1-\delta_{27} & 0 \\ 0 & 1+\delta_{23} & 0 & -1-\delta_{43} & 0 & 1+\delta_{63} & 0 & -1-\delta_{83} \\ 1-\delta_{41} & 0 & -1+\delta_{43} & 0 & 1-\delta_{45} & 0 & 1-\delta_{47} & 0 \\ 0 & 1+\delta_{25} & 0 & 1+\delta_{45} & 0 & 1+\delta_{65} & 0 & -1-\delta_{85} \\ -1+\delta_{61} & 0 & 1-\delta_{63} & 0 & 1-\delta_{65} & 0 & -1+\delta_{67} & 0 \\ 0 & 1+\delta_{27} & 0 & 1+\delta_{47} & 0 & -1-\delta_{67} & 0 & -1-\delta_{87} \\ 1-\delta_{81} & 0 & -1+\delta_{83} & 0 & -1+\delta_{85} & 0 & -1+\delta_{87} & 0 \end{pmatrix}. \quad \text{(A1)}$$

The spatial decay factor of the intercell hopping amplitude is

$$f(r_{jk})=e^{1-r_{jk}}, \quad \text{(A2)}$$

where $r_{jk} = l_0$, l_1, or l_2. l_0 is the side length of the square or rhombus, l_1 is the length of the diagonal of the square, and l_2 is the length of the short diagonal of the rhombus in Ammann–Beenker (AB) tiling quasicrystals. Here $l_0 = 1$.

The term related to the angle between cells is

$$\Omega(\phi_{jk})=\begin{pmatrix} 0 & \omega_{\frac{3\pi}{4}}(\phi_{jk}) & 0 & \omega_{\pi}(\phi_{jk}) & 0 & -\omega_{-\frac{3\pi}{4}}(\phi_{jk}) & 0 & \omega_{-\frac{\pi}{2}}(\phi_{jk}) \\ \omega_{-\frac{\pi}{4}}(\phi_{jk}) & 0 & \omega_{\pi}(\phi_{jk}) & 0 & \omega_{-\frac{3\pi}{4}}(\phi_{jk}) & 0 & \omega_{-\frac{\pi}{2}}(\phi_{jk}) & 0 \\ 0 & \omega_{0}(\phi_{jk}) & 0 & -\omega_{-\frac{3\pi}{4}}(\phi_{jk}) & 0 & \omega_{-\frac{\pi}{2}}(\phi_{jk}) & 0 & -\omega_{-\frac{\pi}{4}}(\phi_{jk}) \\ \omega_{0}(\phi_{jk}) & 0 & -\omega_{\frac{\pi}{4}}(\phi_{jk}) & 0 & \omega_{-\frac{\pi}{2}}(\phi_{jk}) & 0 & \omega_{-\frac{\pi}{4}}(\phi_{jk}) & 0 \\ 0 & \omega_{\frac{\pi}{4}}(\phi_{jk}) & 0 & \omega_{\frac{\pi}{2}}(\phi_{jk}) & 0 & \omega_{-\frac{\pi}{4}}(\phi_{jk}) & 0 & -\omega_{0}(\phi_{jk}) \\ -\omega_{\frac{\pi}{4}}(\phi_{jk}) & 0 & \omega_{\frac{\pi}{2}}(\phi_{jk}) & 0 & \omega_{\frac{3\pi}{4}}(\phi_{jk}) & 0 & -\omega_{0}(\phi_{jk}) & 0 \\ 0 & \omega_{\frac{\pi}{2}}(\phi_{jk}) & 0 & \omega_{\frac{3\pi}{4}}(\phi_{jk}) & 0 & -\omega_{\pi}(\phi_{jk}) & 0 & -\omega_{\frac{\pi}{4}}(\phi_{jk}) \\ \omega_{\frac{\pi}{2}}(\phi_{jk}) & 0 & -\omega_{\frac{3\pi}{4}}(\phi_{jk}) & 0 & -\omega_{\pi}(\phi_{jk}) & 0 & -\omega_{-\frac{3\pi}{4}}(\phi_{jk}) & 0 \end{pmatrix}, \quad \text{(A3)}$$

where

$$\omega_{\theta}(\phi_{jk})=\varepsilon_{\theta}(\phi_{jk})\Phi_{\theta}(\phi_{jk}), \quad \text{(A4)}$$

where $\varepsilon_{\theta}(\phi_{jk})=\begin{cases}1, & |\phi_{jk}-\theta|\le\dfrac{\pi}{8}\\ 0, & |\phi_{jk}-\theta|>\dfrac{\pi}{8}\end{cases}$, $\Phi_{\theta}(\phi_{jk})=\cos(\phi_{jk}-\theta)$, ϕ_{jk} is the angle between the

hopping direction ($j \to k$) and the positive horizontal direction.

Moreover, the part of the Hamiltonian related to dissipation δH_{D} in Eq. (12) in the main text is

$$\delta H_{\mathrm{D}} = \sum_j c_j^{\dagger} \begin{pmatrix} 0 & \delta_{21} & 0 & \delta_{41} & 0 & -\delta_{61} & 0 & \delta_{81} \\ -\delta_{21} & 0 & -\delta_{23} & 0 & -\delta_{25} & 0 & -\delta_{27} & 0 \\ 0 & \delta_{23} & 0 & -\delta_{43} & 0 & \delta_{63} & 0 & -\delta_{83} \\ -\delta_{41} & 0 & \delta_{43} & 0 & -\delta_{45} & 0 & -\delta_{47} & 0 \\ 0 & \delta_{25} & 0 & \delta_{45} & 0 & \delta_{65} & 0 & -\delta_{85} \\ \delta_{61} & 0 & -\delta_{63} & 0 & -\delta_{65} & 0 & \delta_{67} & 0 \\ 0 & \delta_{27} & 0 & \delta_{47} & 0 & -\delta_{67} & 0 & -\delta_{87} \\ -\delta_{81} & 0 & \delta_{83} & 0 & \delta_{85} & 0 & \delta_{87} & 0 \end{pmatrix} c_j . \qquad \text{(A5)}$$

B. Kitaev formula

In order to shorten the calculation time, we use another form of the Kitaev formula to calculate the Chern numbers for band α:[1]

$$C_\alpha = 12\pi i(\mathrm{Tr}(\bar{\boldsymbol{A}}P^\alpha\bar{\boldsymbol{B}}P^\alpha\bar{\boldsymbol{C}}P^\alpha) - \mathrm{Tr}(\bar{\boldsymbol{A}}P^\alpha\bar{\boldsymbol{C}}P^\alpha\bar{\boldsymbol{B}}P^\alpha)), \qquad \text{(B1)}$$

where $\bar{\boldsymbol{A}}$, $\bar{\boldsymbol{B}}$ and $\bar{\boldsymbol{C}}$ are the projection operators of regions $\boldsymbol{A}$, $\boldsymbol{B}$ and $\boldsymbol{C}$ in Fig. 1(a), ($\bar{\boldsymbol{A}}+\bar{\boldsymbol{B}}+\bar{\boldsymbol{C}}=\mathbf{1}$, $\mathbf{1}$ is the identity matrix). Under the open boundary condition, it is difficult to completely separate the bulk states from the topological edge states (TESs). In order to avoid the influence of the TESs on the calculation of the Chern numbers for bulk bands, we set the elements of the region close to the outer boundary in the projection operator P^α to be 0, with reference to the calculation of Chern numbers in the hyperbolic model.[2] For the quasicrystal with the regular octagon outer boundary, the distance from the site to the center of the quasicrystal is d_1, and the distance from the center of the quasicrystal to its outer boundary is d_0. The region close to the outer boundary of the quasicrystal is defined as: $d_1/d_0 > 0.85$.

C. Local Chern marker

In addition to the Kitaev formula, it is also possible to calculate the real-space

Chern numbers in a quasicrystal with the local Chern marker.[3] The local Chern marker is modified below for non-Hermitian systems. In a non-Hermitian system, the local Chern number for band α at the lattice site $\boldsymbol{r}_i$ can be defined as

$$\mathbb{C}^{\alpha}(\boldsymbol{r}_i) = -4\pi \,\mathrm{Im}\left[\sum_{\boldsymbol{r}_j} \langle \boldsymbol{r}_i | \hat{x}_Q | \boldsymbol{r}_j \rangle \langle \boldsymbol{r}_j | \hat{y}_P | \boldsymbol{r}_i \rangle\right], \tag{C1}$$

where $\langle \boldsymbol{r}_i | \hat{x}_Q | \boldsymbol{r}_j \rangle = \sum_{\boldsymbol{r}_k} Q^{\alpha}(\boldsymbol{r}_i, \boldsymbol{r}_k) x_k P^{\alpha}(\boldsymbol{r}_k, \boldsymbol{r}_j)$ and $\langle \boldsymbol{r}_j | \hat{y}_P | \boldsymbol{r}_i \rangle = \sum_{\boldsymbol{r}_k} P^{\alpha}(\boldsymbol{r}_j, \boldsymbol{r}_k) y_k Q^{\alpha}(\boldsymbol{r}_k, \boldsymbol{r}_i)$. P^{α} and Q^{α} are the projection operators of a band, where $P^{\alpha}(\boldsymbol{r}_i, \boldsymbol{r}_j) = \sum_{n\in\alpha} \langle \boldsymbol{r}_i | nR \rangle \langle nL | \boldsymbol{r}_j \rangle$ and $Q^{\alpha}(\boldsymbol{r}_i, \boldsymbol{r}_j) = \sum_{n\notin\alpha} \langle \boldsymbol{r}_i | nR \rangle \langle nL | \boldsymbol{r}_j \rangle$. The average Chern number for band α is $C_D^{\alpha} = \frac{1}{\pi r_D^2} \sum_{\boldsymbol{r}_i} \mathbb{C}^{\alpha}(\boldsymbol{r}_i)$, where r_D is the radius of the selected region D.

In order to shorten the calculation time, the local Chern number can be changed to the matrix calculation:

$$C_{\alpha}^{D} = \frac{4\pi i}{\pi r_D^2} \mathrm{Tr}(Q^{\alpha} X P^{\alpha} P^{\alpha} Y Q^{\alpha}) = \frac{4\pi i}{\pi r_D^2} \mathrm{Tr}(Q^{\alpha} X P^{\alpha} Y Q^{\alpha}), \tag{C2}$$

where X and Y are coordinate operators for x- and y-coordinates. Similar to Sec. B, when tracing, only the elements on the diagonal of the matrix that are not close to the outer boundary are summed (in this case, $d_1/d_0 \leq 0.85$). In Fig. 2(a) in the main text, the average local Chern numbers are $C_1 = C_4 \approx -0.90$ and $C_2 = C_3 \approx 0.90$. It is worth noting that the Chern number studied by the Kitaev formula is more rubust than that studied by the local Chern marker.[3]

D. Bulk states in quasicrystals

In order to study the Chern numbers for the bulk bands, it is necessary to distinguish the bulk states from the TESs. The method for obtaining pure bulk states is shown in Fig. D1. Since the quasicrystal structure is not periodic, it is impossible to remove all TESs by a periodic boundary condition (PBC) to obtain pure bulk states, but it is still possible to consider the quasicrystal structure as a unit to construct a periodic structure (as shown in Fig. D1(a)) and obtain approximate bulk bands (as shown in Figs.

D1(b) and D1(c)).

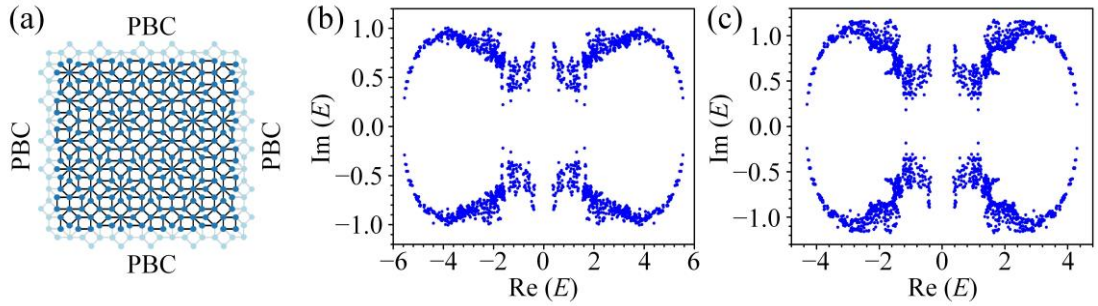

Fig. D1 (a) Schematic of constructing a periodic structure with the AB tiling quasicrystal (the light-colored region is the equivalent hoppings set for the boundary when constructing a periodic structure). (b) Complex energy spectrum of Fig. D1(a); δ and t in the Hamiltonian H are the same as those of Fig. 2(a) in the main text. (c) Complex energy spectrum of Fig. D1(a); δ and t in the Hamiltonian H are the same as those of Fig. 3(e) in the main text.

The eigenstates in the complex energy spectra in Figs. D1(b) and D1(c) correspond to the bulk states without skin effect. According to Figs. D1(b) and D1(c), it is possible to distinguish the bulk states with PBC along both directions from the TESs (see Fig. 2(a) in the main text and Fig. E1 below). In fact, since there is no skin effect for the bulk, it is also possible to distinguish the bulk states from the TESs localized at corners due to skin effect according to the eigenfield distribution.[4–7]

E. Additional data to Fig. 3 in the main text

For the localization effect of topological states with the quadrilateral outer boundary, the situations for the kite and square outer boundary are analyzed in the main text (as shown in Figs. 3(a) and 3(b)). In order to verify the localization of topological states for the parallelogram outer boundary, the complex energy spectrum of the AB tiling quasicrystal and the eigenfield of its TES for the parallelogram outer boundary are calculated (as shown in Fig. E1(a)). It can be seen that the eigenfield of the TES is localized at the corners due to the skin effect, i.e., the hybrid skin-topological effect (HSTE) is realized.

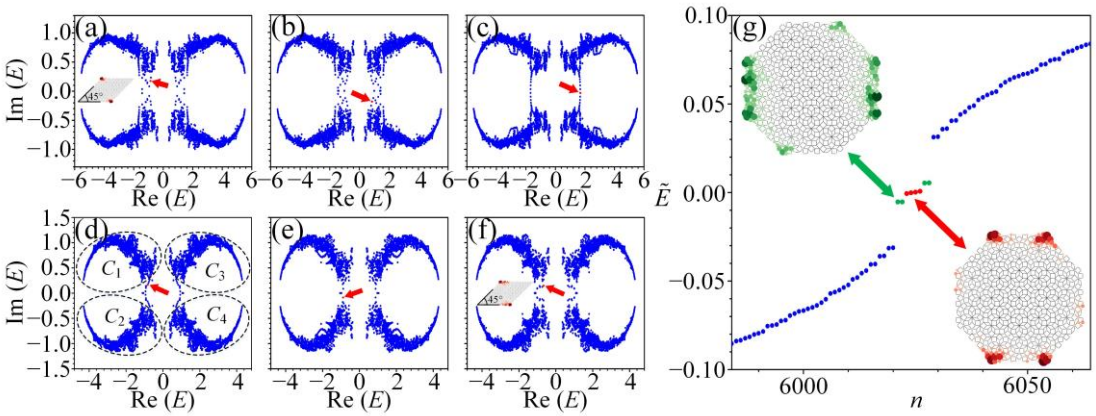

Fig. E1 (a)–(c) Complex energy spectra of the models with different quadrilateral outer boundaries; δ and t in the Hamiltonian H are the same as those of Fig. 2(a) in the main text. (a) For the parallelogram outer boundary, the complex energy spectrum and the normalized eigenfield for the red dot marked by the red arrow. (b) and (c) Complex energy spectra of Figs. 3(a) and 3(b) in the main text, where the red dots marked by the red arrows are corresponding to the eigenvalues of the eigenfields in the main text. (d)–(g) Complex energy spectra of the models with different outer boundaries; δ and t in the Hamiltonian H are the same as those of Fig. 3(e) in the main text. (d) Complex energy spectrum of Fig. 3(e) in the main text. The Chern numbers for the bulk bands in the dashed circles are C_1, C_2, C_3, and C_4. The red dot marked by the red arrow is corresponding to the eigenvalue of the eigenfield in the main text. (e) Complex energy spectrum of Fig. 3(f) in the main text, where the red dot marked by the red arrow is corresponding to the eigenvalue of the eigenfield in the main text. (f) Complex energy spectrum and the normalized eigenfield for the red dot marked by the red arrow, when the outer boundary of Fig. 3(f) in the main text is rotated 90°. (g) Energy spectrum of $\tilde{H}(E_r)$ as a function of the eigenvalue index n when E_r is the same as the eigenvalue of Fig. 3(e) in the main text. The zero-energy (marked by the red dots) eigenfield is shown in the inset in the bottom right corner, and the eigenfield for the eigenvalues adjacent to the zero-energy eigenvalues (marked by the green dots) is shown in the inset in the top left corner.

The complex energy spectra of Figs. 3(a), 3(b), 3(e) and 3(f) in the main text are shown in Figs. E1(b)–E1(e), respectively, revealing the emergence of TESs in the bulk gaps. However, the skin effect on TESs cannot be analyzed only according to the complex energy spectrum, and the analysis needs to be combined with the eigenfield or

auxiliary Hamiltonian (see the main text). In Fig. E1(d), the Chern numbers for bulk bands are calculated according to Eq. (4) in the main text: $C_1 = C_4 \approx -0.99$ and $C_2 = C_3 \approx 0.99$. The existence of the TESs is ensured by the nontrivial topological invariants. In addition, when the outer boundary of Fig. 3(f) in the main text is rotated 90°, the Hamiltonian for TESs will change because the system is only twofold rotationally symmetric, so the energy spectra of the TESs in Figs. E1(e) and E1(f) are also different.

In the main text, under the action of HSTE, the eigenfield of the TES is localized at two corners in Fig. 3(e). In order to further analyze the HSTE in Fig. 3(e), the auxiliary Hamiltonian is analyzed below. As shown in Fig. E1(g), four degenerate zero-energy eigenstates appear in the edge gap of the auxiliary Hamiltonian $\tilde{H}(E_r)$ (as shown by the red dots). It can be seen from the eigenfield that these zero-energy eigenstates are indeed corner states (as shown in the inset in the bottom right corner in Fig. E1(g)). In other words, the skin effect indeed acts on the TESs of the original Hamiltonian H. Different from Fig. 2(c) in the main text, fourfold degenerate zero-energy eigenstates appear in Fig. E1(g), and the corresponding eigenfields are only localized at four corners of the regular octagon, while the eightfold degenerate zero-energy eigenstates appear in Fig. 2(c). Moreover, the four eigenstates adjacent to the zero-energy eigenstates (as shown by the green dots) become edge states (as shown in the inset in the top left corner in Fig. E1(g)). According to these edge states for the auxiliary Hamiltonian, the other four corners are barely affected by the skin effect.

F. HSTE in disordered cases

For $\omega = 0.2$ or 0.5 (ω is the parameter related to disorder), the complex energy spectra of the system with specific δ and t and the eigenfields for HSTE are shown in Fig. F1.

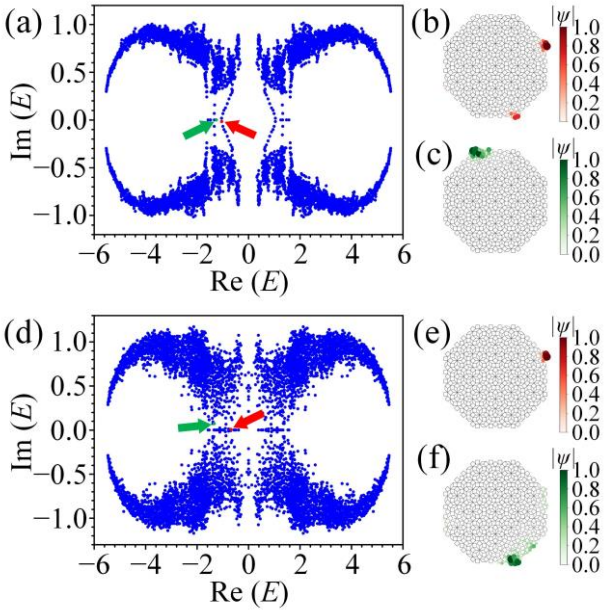

Fig. F1 Models with the regular octagon outer boundary; $\delta_{21} = \delta_{43} = \delta_{65} = \delta_{87} = \delta_{61} = \delta_{25} = \delta_{83} = \delta_{47} = 0.3 + U$, $\delta_{23} = \delta_{45} = \delta_{67} = \delta_{81} = \delta_{27} = \delta_{63} = \delta_{41} = \delta_{85} = 0.8 + U$, and $t = 1.2$; U is a random number chosen uniformly in the range $[-\omega, \omega]$ in the Hamiltonian H. The complex energy spectra; the normalized eigenfields for the red and green dots marked by arrows in the complex energy spectra: (a)–(c) $\omega = 0.2$; (d)–(f) $\omega = 0.5$.

When $\omega = 0.2$ or 0.5, there are states that realizes HSTE in the bulk gap of the complex energy spectrum (as shown in Figs. F1(a) and F1(d)), and the corner localization of these states may be different (as shown in Figs. F1(b), F1(c), F1(e), and F1(f)). Moreover, considering the above results from the point of view of auxiliary Hamiltonian, when the reference energys E_r are consistent with the eigenvalues of the above TESs, the corner states of the auxiliary Hamiltonian $\tilde{H}(E_r)$ corresponding to Figs. F1(a) and F1(d) are robust to disorder, which is similar to the corner states of the higher-order topological Anderson insulator.[8] It is evident that the HSTE in the quasicrystals can also remain stable for strong disorder, while the corner localization may change for different eigenvalues, which is helpful to further regulate the localization with HSTE.

G. HSTE with four-site cells in AB tiling quasicrystals

The AB tiling quasicrystals with four-site cells can also realize HSTE, and the analysis is shown in Fig. G1.

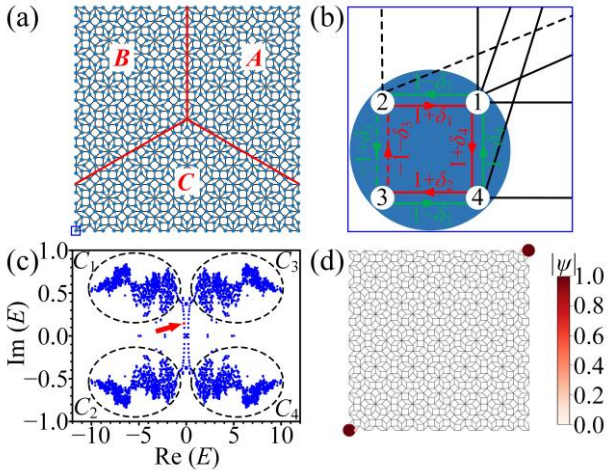

Fig. G1 (a) AB tiling quasicrystal with a square outer boundary. The inner boundary is set for calculating the Chern numbers for the bulk bands with the Kitaev formula. The three regions divided by the inner boundary are marked by ***A***, ***B***, and ***C***. (b) Schematic of the four-site cell and the hoppings (here is a magnification of the blue box in the bottom left corner in Fig. G1(a)). When $\delta_1 = \delta_2 = 0.3$, $\delta_3 = \delta_4 = -1$, $t = 0.85$: (c) the complex energy spectrum. The Chern numbers for the bulk bands in the dashed circles are C_1, C_2, C_3, and C_4; (d) the normalized eigenfield for the red dot marked by the red arrow in Fig. G1(c).

As shown in Fig. G1(a), a square outer boundary is set for the quasicrystal, where each point represents a cell and each cell contains four sites (see Fig. G1(b)). The intercell hoppings are introduced on the sides of the square units, as well as the sides and shorter diagonals of the rhomboid units (similar to Figs. 1(c) and 1(d) in the main text, but no hoppings are introduced on the diagonals of the square units, different from the main text). Analog to the two-dimensional square lattice Su–Schrieffer–Heeger (SSH) model realizing HSTE,[4] the nonreciprocal intracell hoppings are introduced (the nonreciprocity is achieved using a non-zero δ, with δ quantifying the nonreciprocal hopping between two sites).

The form of Hamiltonian H of the system is the same as that in the main text (i.e., Eqs. (1), (2), and (3)), but the specific contents of T, t, $f(r_{jk})$, and $\Omega(\phi_{jk})$ are different:

T is the intracell hopping of a cell,

$$T=\Gamma_1+\Gamma_2+i\frac{\delta_1+\delta_2}{2}\Gamma_3+i\frac{\delta_1-\delta_2}{2}\Gamma_4-i\frac{\delta_3+\delta_4}{2}\Gamma_5+i\frac{\delta_3-\delta_4}{2}\Gamma_6, \tag{G1}$$

where $\Gamma_1=\tau_2\tau_2$, $\Gamma_2=\tau_0\tau_1$, $\Gamma_3=\tau_0\tau_2$, $\Gamma_4=\tau_3\tau_2$, $\Gamma_5=\tau_2\tau_1$, and $\Gamma_6=\tau_1\tau_2$. $\tau_{1,2,3}$ are the Pauli matrices, and τ_0 is the identity matrix.

t is the intercell hopping amplitude, and $f(r_{jk})$ is the spatial decay factor of the intercell hopping amplitude,

$$f(r_{jk})=e^{1-r_{jk}}, \tag{G2}$$

where $r_{jk}=l_0$ or l_1. l_0 is the side length of the square or rhombus, and l_1 is the length of the short diagonal of the rhombus in the AB tiling quasicrystals. Here $l_0=1$.

$\Omega(\phi_{jk})$ is a term related to the angle between cells,

$$\Omega(\phi_{jk})=\cos\phi_{jk}\Gamma_2-\left|\cos\phi_{jk}\right|i\Gamma_4-\sin\phi_{jk}\Gamma_1-\left|\sin\phi_{jk}\right|i\Gamma_6, \tag{G3}$$

where ϕ_{jk} is the angle between the hopping direction ($j\rightarrow k$) and the positive horizontal direction.

According to Eq. (4) in the main text, the Chern numbers for the bulk bands in Fig. G1(c) are $C_1=C_4\approx-0.99$ and $C_2=C_3\approx0.99$, and the nontrivial topological invariants ensure the existence of the TESs. In Fig. G1(d), the eigenfield of the TES is localized at the corners due to the skin effect, i.e., the HSTE is realized.

References

[1] Kitaev A 2006 *Ann. Phys.* **321** 2

[2] Urwyler D M, Lenggenhager P M, Boettcher I, Thomale R, Neupert T and Bzdušek T 2022 *Phys. Rev. Lett.* **129** 246402

[3] He A L, Ding L R, Zhou Y, Wang Y F and Gong C D 2019 *Phys. Rev. B* **100** 214109

[4] Lee C H, Li L and Gong J 2019 *Phys. Rev. Lett.* **123** 016805

[5] Li Y, Liang C, Wang C, Lu C and Liu Y C 2022 *Phys. Rev. Lett.* **128** 223903

[6] Zhu W and Gong J 2022 *Phys. Rev. B* **106** 035425

[7] Sun J, Li C A, Feng S and Guo H 2023 *Phys. Rev. B* **108** 075122

[8] Peng T, Hua C B, Chen R, Liu Z R, Xu D H and Zhou B 2021 *Phys. Rev. B* **104** 245302